Supplement of

Exploring the sources of light-absorbing carbonaceous aerosols by integrating observational and modeling results: insights from Northeast China

Yuan Cheng[1], Xu-bing Cao[1], Sheng-qiang Zhu[2], Zhi-qing Zhang[1], Jiu-meng Liu[1,*], Hong-liang Zhang[2], Qiang Zhang[3] and Ke-bin He[4]

[1] State Key Laboratory of Urban Water Resource and Environment, School of Environment, Harbin Institute of Technology, Harbin, 150090, China

[2] Department of Environmental Science and Engineering, Fudan University, Shanghai 200438, China

[3] Ministry of Education Key Laboratory for Earth System Modeling, Department of Earth System Science, Tsinghua University, Beijing, 100084, China

[4] State Key Joint Laboratory of Environment Simulation and Pollution Control, School of Environment, Tsinghua University, Beijing, 100084, China

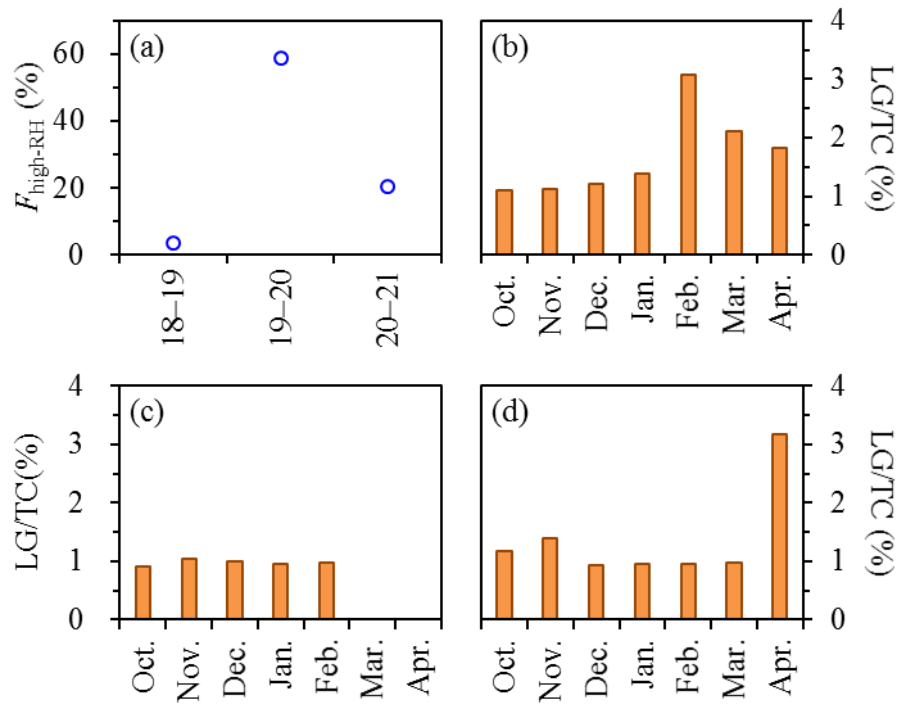* Corresponding author. Jiu-meng Liu (jiumengliu@hit.edu.cn).

Figure S1. (a) $F_{high-RH}$, the fractions of wintertime samples with RH above 80%, for the 2018–2019 (18–19), 2019–2020 (19–20) and 2020–2021 (20–21) campaigns. **(b–d)** Monthly-averaged LG to TC ratios (on a basis of carbon mass) for the three campaigns, respectively. During the 2018–2019 and 2020–2021 campaigns, the LG/TC ratios peaked in February and April, respectively. Both months were characterized by intensive fire hotspots in and around Harbin, pointing to prevalence of agricultural fires.
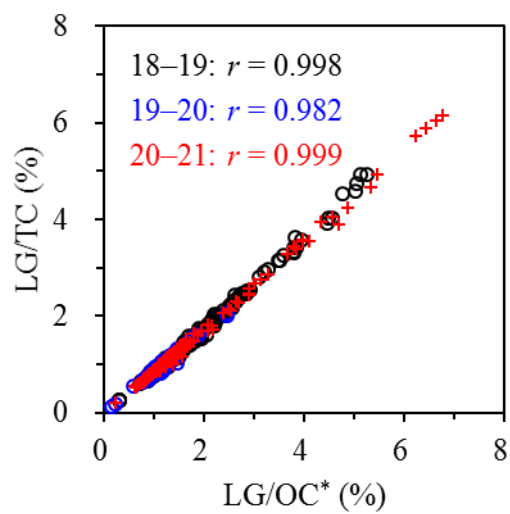
Figure S2. Dependences of LG/TC on LG/OC* for the three campaigns. The two ratios exhibited strong linear correlations as indicated by the close-to-one r values.
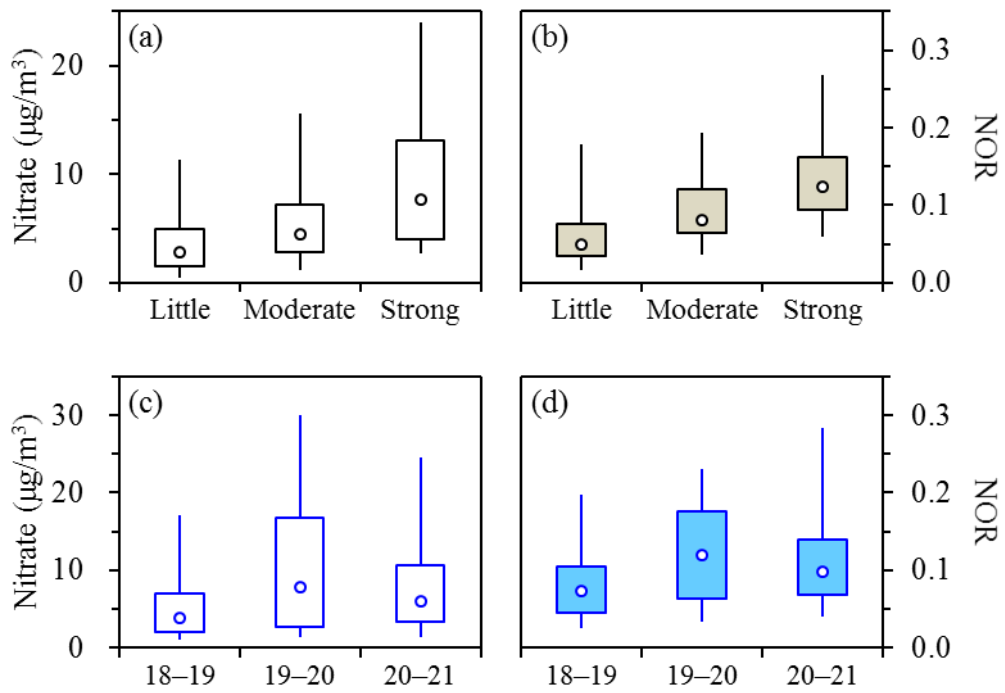
Figure S3. Comparisons of **(a)** nitrate and **(b)** NOR across three cases with increasing impacts of agricultural fires for the 2018–2019 campaign, and comparisons of **(c)** nitrate and **(d)** NOR across the three campaigns.
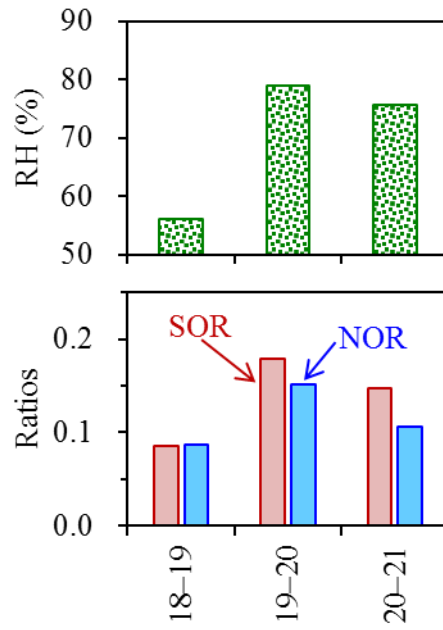
Figure S4. Average RH (upper panel), SOR and NOR (lower panel) for the winters of 18–19, 19–20 and 20–21.
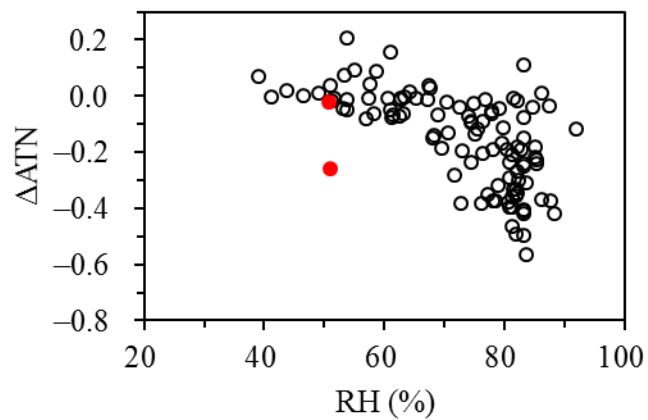
Figure S5. Dependence of ΔATN on RH for the 2019–2020 campaign. Only two samples were strongly impacted by agricultural fires, as highlighted by the red circles.
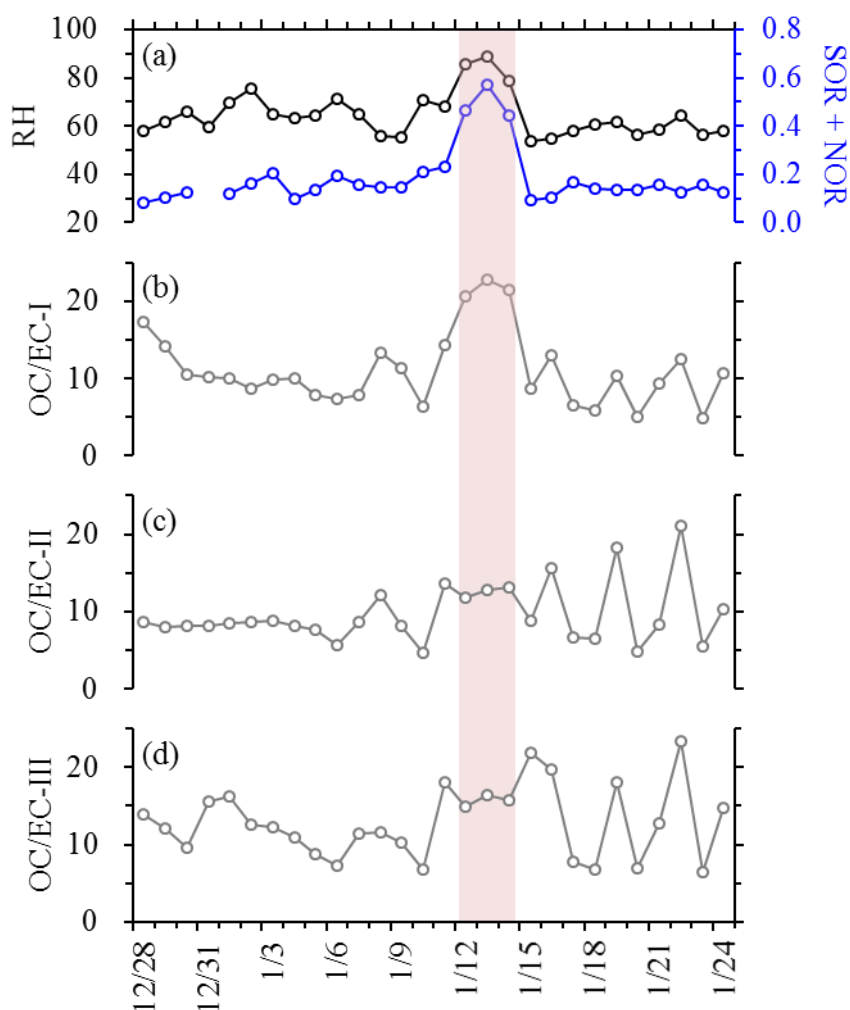
Figure S6. Temporal variations of **(a)** RH and SOR + NOR, **(b)** OC/EC-I, **(c)** OC/EC-II and **(d)** OC/EC-III for samples during the 2018–2019 winter period with insignificant influence of agricultural fires. The shadowed area highlights three distinct samples characterized by high RH and enhanced formation of secondary aerosols. OC/EC-I was derived from OC and EC measured by the untreated sample using NIOSH. OC/EC-II was calculated by $EC_{extracted,\ IMPROVE-A}$ and the corresponding OC (i.e., $TC_{untreated} - EC_{extracted,\ IMPROVE-A}$). OC/EC-III was determined similarly based on NIOSH. Obviously, OC/EC-II and OC/EC-III exhibited poor accordance with secondary aerosol formation. For the OC/EC-I ratio, it was elevated for not only the high-RH period but also some low-RH samples, prohibiting the use of it as a robust indicator for the RH-dependent enhancement of SOA production.
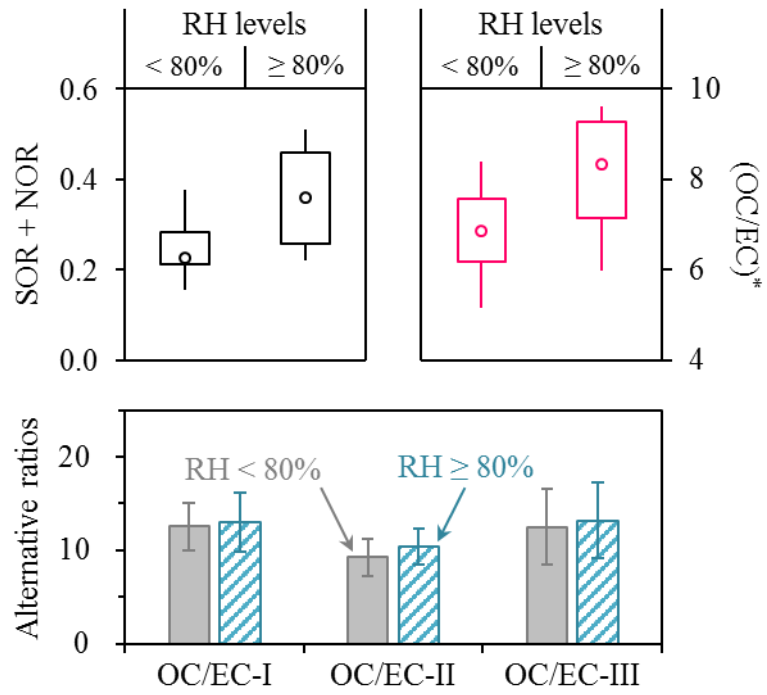
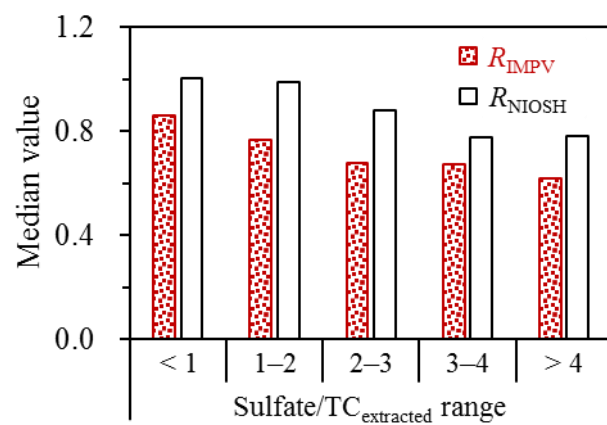**Figure S7.** The same as Figure 4 in the main manuscript but for January 2021.

Figure S8. Comparisons of R_{IMPV} and R_{NIOSH} across different sulfate/TC$_{extracted}$ ranges for the samples with little fire impact. Results from all the three campaigns were involved.
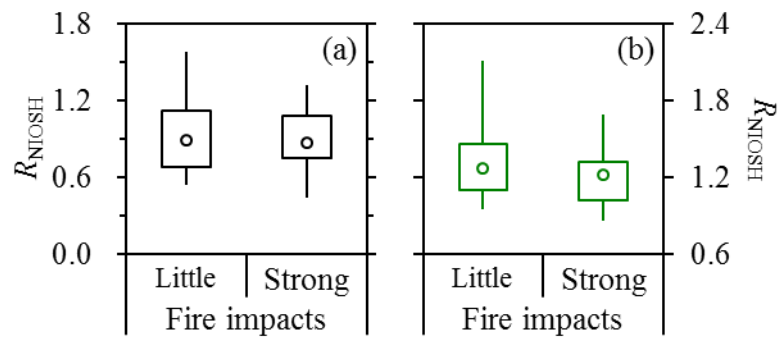
Figure S9. **(a)** Comparison of R_{NIOSH} between the 2018–2019 samples with strong impacts of agricultural fires (as indicated by "Strong") and those with the same sulfate/TC$_{extracted}$ range but little fire impact (as indicated by "Little"). **(b)** The same as (a) but for 2020–2021.
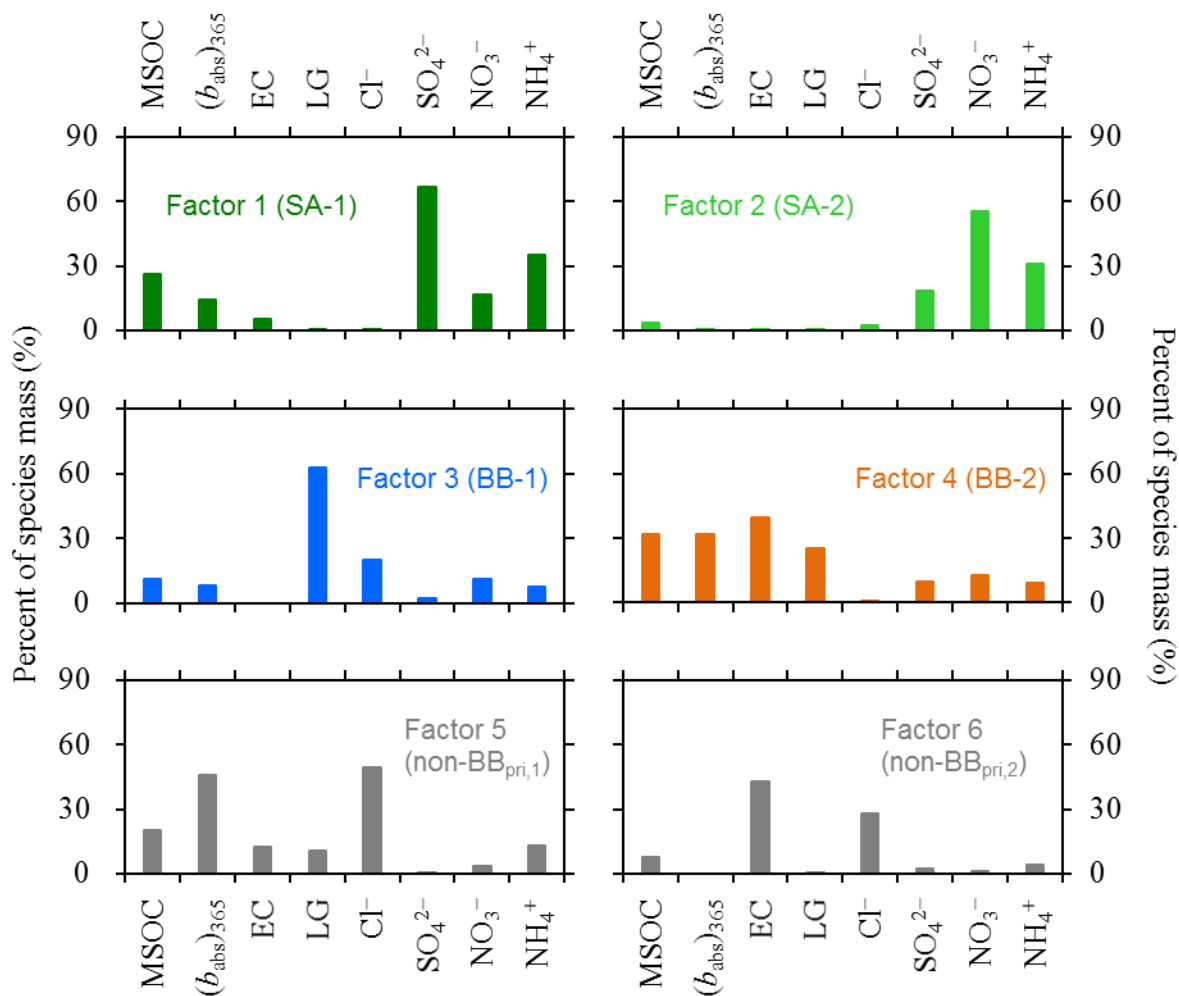
Figure S10. Source profiles resolved by PMF. The first two factors (i.e., SA-1 and SA-2) were considered secondary, since they had little EC but the majority of secondary ions. The third and fourth factors (i.e., BB-1 and BB-2) were attributed to primary emissions from biomass burning, as ~90% of levoglucosan was apportioned into these two factors whereas none of them was a major contributor to secondary ions. The last two factors (i.e., non-BB$_{pri,1}$ and non-BB$_{pri,2}$) were inferred to represent primary emissions from non-BB sources, due to their dominant contributions to EC and chloride.
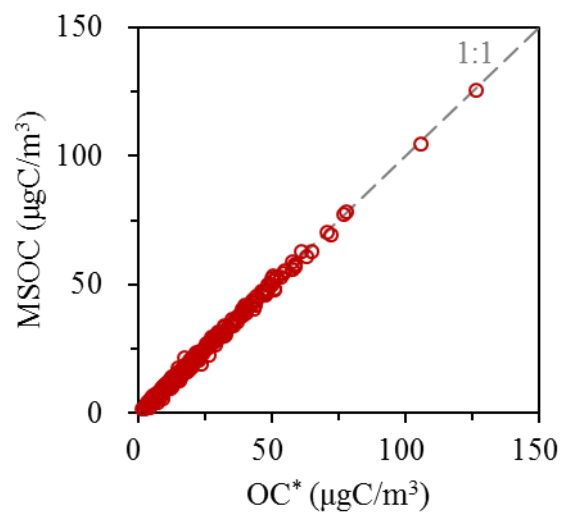
Figure S11. Dependence of MSOC on OC*, with the 1:1 line also included. Linear regression of MSOC on OC* led to a close-to-one slope of 0.99 ± 0.00 (intercept was set as zero; r = 0.998). Results from all the three campaigns were involved.
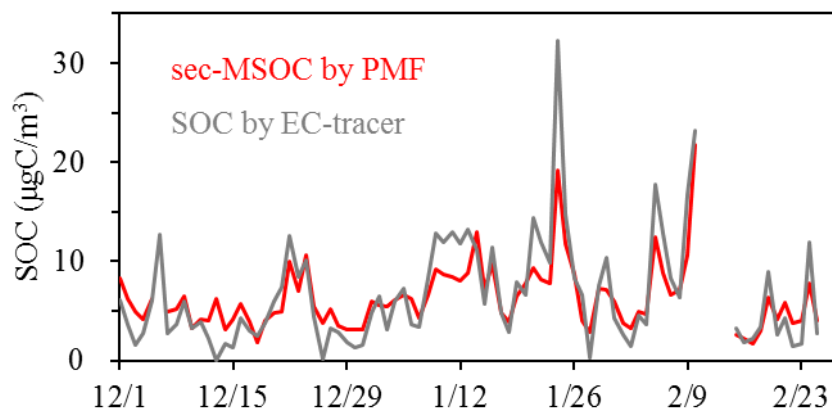
Figure S12. Variations of SOC derived from different approaches for the 2020–2021 winter. SOC was determined as secondary MSOC (i.e., sec-MSOC) based on PMF. In addition, SOC was also estimated by the EC-tracer method, using OC^* and EC^* (i.e., the IMPROVE-A results from the untreated samples); in this approach, SOC was calculated as $OC - EC \times (OC/EC)_{min}$, where $(OC/EC)_{min}$ indicates the minimum OC to EC ratio. SOC resolved by the two approaches showed similar patterns of temporal variation and comparable mass concentrations, leading to a strong linear correlation ($r = 0.91$). SOC was not estimated for the samples strongly impacted by firework emissions during the Chinese New Year Period.